

HiResCAM: Explainable Multi-Organ Multi-Abnormality Prediction in 3D Medical Images

Rachel Lea Draelos
Computer Science Department
Duke University
rlb61@duke.edu

Lawrence Carin
ECE Department
Duke University
lcarin@duke.edu

Abstract

Understanding model predictions is critical in health-care, to facilitate rapid real-time verification of model correctness and to guard against the use of models that exploit confounding variables. Motivated by the need for explainable models, we address the challenging task of explainable multiple abnormality classification in volumetric medical images. We propose a novel attention mechanism, HiResCAM, that highlights relevant regions within each volume for each abnormality queried. We investigate the relationship between HiResCAM and the popular model explanation method Grad-CAM, and demonstrate that HiResCAM yields better performance on abnormality localization and produces explanations that are more faithful to the underlying model. Finally, we introduce a mask loss that leverages HiResCAM to require the model to predict abnormalities based on only the organs in which those abnormalities appear. Our innovations achieve a 37% improvement in explanation quality, resulting in state-of-the-art weakly supervised organ localization of abnormalities in the RAD-ChestCT data set of 36,316 CT volumes. We also demonstrate on PASCAL VOC 2012 the different properties of HiResCAM and Grad-CAM on natural images. Overall, this work advances convolutional neural network explanation approaches and the clinical applicability of multi-abnormality modeling in volumetric medical images.

1. Introduction

Automated interpretation of medical images with machine learning has the potential to revolutionize the field of radiology. However, machine learning systems have not yet been adopted on a large scale in clinical practice [3]. One barrier to adoption is trust [40, 47]. Most medical imaging models are based on convolutional neural networks, which are “black box” models unless additional steps are taken to

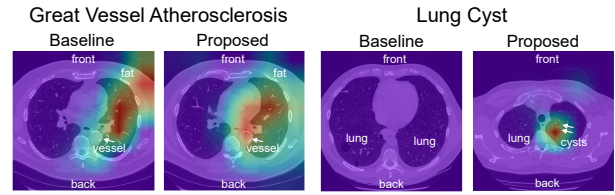


Figure 1. An example of improved chest CT scan explanations via our proposed attention mechanism HiResCAM and proposed mask loss, relative to a baseline using Grad-CAM and no mask loss. For the label “great vessel atherosclerosis,” the baseline visualization includes a strong focus on the fat layer surrounding the patient’s body; the model is likely using obesity as a proxy for atherosclerosis. The proposed model correctly focuses on the atherosclerosis itself, visible as a rim of calcifications around the great vessel. For lung cyst, the baseline explanation fails, while the proposed model explanation highlights cystic areas of the lungs. Anatomy annotations were added for clarity. Best viewed in color.

improve explainability [4].

An explainable model in computer vision indicates which regions of the image contribute to its predictions [4]. Explainability is critical in medical imaging to detect situations where a model leverages aspects of the data that are correlated with an outcome but inappropriate for prediction. Zech *et al.* [63] used class activation mapping [65] to reveal that a CNN trained to predict pneumonia from chest radiographs leveraged non-medical features to make the pneumonia prediction. Specifically, the CNN identified differences in metal tokens, postprocessing, and compression artefacts which identified the hospital system of origin, a highly effective indicator of pneumonia risk due to differing frequencies of pneumonia among the patient populations. Furthermore, a “model” consisting of sorting the radiographs by hospital system achieved an AUROC of 0.861, illustrating that high performance alone does not guarantee that a model is faithful to expected medical reasoning. This behavior is analogous to natural image classifiers detecting

boats via water, trains via rails, or horses via a copyright watermark [33, 34]. It is thus critical to seek insight into how models make their predictions.

In this work, we consider explainable multilabel classification in volumetric medical images. Our contributions include:

- A new region-focused attention mechanism, High-Resolution Class Activation Mapping (HiResCAM), that identifies the locations in the input volume that most contribute to prediction of each abnormality.
- An approach to obtain pixel-level allowed regions for each abnormality without any manual labeling, by combining unsupervised multi-organ segmentation with location information in radiology reports.
- A mask loss that leverages HiResCAM and the allowed regions during training to encourage the model to predict abnormalities from within the organs in which they are found.

Our combined innovations yield state-of-the-art performance on explainable multi-abnormality prediction in 3D medical images.

2. Related Work

Abnormality prediction in chest CT scans. CT scans are used to diagnose and monitor numerous conditions, including cancer [51], injuries [43], and lung disease [15, 46]. CT scans and natural images differ significantly. Natural images are typically 2D RGB images in which each pixel belongs to only one class and the colors, shapes, and textures of each class are distinct enough for the average human to appreciate the difference (*e.g.* “cat” vs. “dog”). In contrast, CT scans are grayscale volumetric images on the order of 70,000,000 pixels each ($\approx 500\times$ larger than natural images), in which each pixel could belong to multiple classes due to physically overlapping diseases. Furthermore, the color, shape, and texture of each class can be challenging to distinguish even for domain experts, due to heterogeneity within one disease and similarities across different diseases [18, 19, 23, 17].

Due to the challenging and time-consuming nature of CT interpretation, there has been substantial interest in developing machine learning models to analyze CT scans. Almost all prior work in CT classification has focused on one abnormality at a time, such as interstitial lung disease [10, 56, 25, 24, 55, 14, 5], lung cancer [6], pneumothorax [39], or emphysema [29].

The only model developed to predict multiple abnormalities simultaneously from one CT volume is CT-Net [18], which was trained and evaluated on the RAD-ChestCT data set of 36,316 CT volumes annotated with 83 whole-volume

abnormality labels each. While CT-Net achieves high performance, its final representation is not interpretable due to an intermediate convolution step over the feature dimension that disrupts the spatial relationship between the representation and the input volume. Our proposed model outperforms CT-Net while providing explainability.

Gradient-based neural network explanation methods. Our proposed attention mechanism, HiResCAM, is part of the family of gradient-based neural network explanation methods [4].

Input-level approaches. Saliency mapping [53], DeconvNets [64], and Guided Backpropagation [54] are gradient-based explanation methods that compute the gradient of the class score with respect to the input image, to visualize important image regions. These methods are identical except for handling of ReLU nonlinearities [42]. Gradient * Input [52] is a related method in which the gradient of the class score with respect to the input is multiplied element-wise against the input itself. Layer-wise relevance propagation (LRP) [7] proceeds layer-by-layer, starting with the output, to redistribute the final score across the pixels of the input layer. While not originally formulated as a gradient-based explanation method, ϵ -LRP is in fact equivalent to Gradient * Input where the gradient is calculated in a modified manner using the ratio between the output and input at each nonlinearity [4]. A limitation of the aforementioned approaches is the “white noise” appearance of the final explanation caused by noisy gradients [8, 42].

Output-level approaches. Class Activation Mapping (CAM) [65] is an explanation method for a particular class of models that consist of convolutions followed by global average pooling over features and one final fully connected layer. The explanations are produced by multiplying the class-specific weights of the final layer by the corresponding feature maps prior to pooling. CAM may be considered a gradient-based method, as the final class-specific weights are the gradient of the score with respect to the feature maps. Grad-CAM [49] is a generalization of CAM, in which gradients are averaged over the spatial dimensions to produce importance weights. The Grad-CAM explanation is a sum of feature maps weighted by the importance weights.

Unlike the input-level approaches, which rely on propagation through all layers back to the level of the original image, CAM and Grad-CAM produce explanations at a layer of the network closer to the output. The low-dimensional explanation is then upsampled for superimposition over the input image, an acceptable step because typical CNNs preserve spatial relationships. Guided Grad-CAM [49] is a Grad-CAM variant obtained via an element-wise product of Guided Backpropagation [54] and Grad-CAM explanations.

Recent work has called into question some gradient-

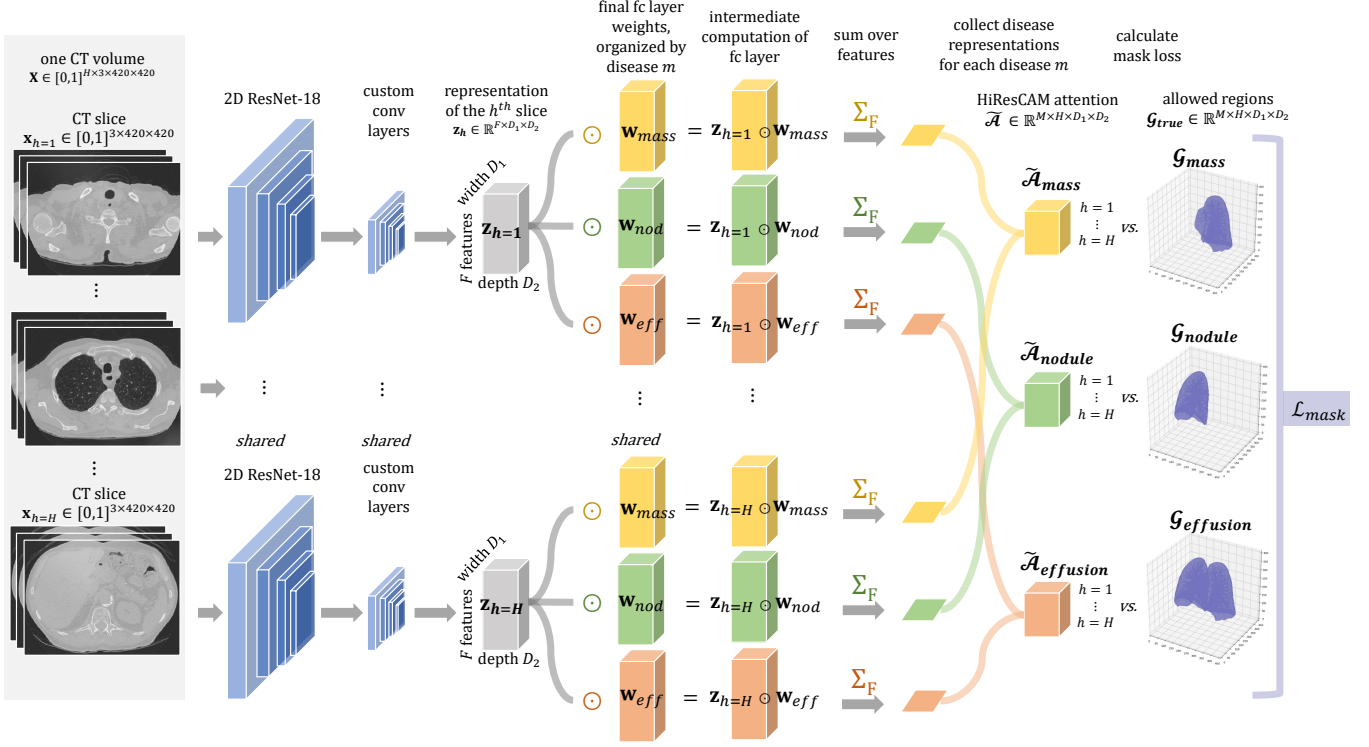


Figure 2. Calculation of the proposed HiResCAM abnormality-specific attention and the proposed mask loss at the last convolutional representation of our AxialNet architecture. A low-dimensional representation \mathbf{z}_h is obtained for each slice $h = 1, \dots, H$ via 2D convolutions on axial slices. A final fully connected layer produces M abnormality scores for each slice (these slice scores are not explicitly shown). A HiResCAM attention map is calculated for each abnormality as the element-wise product of the low-dimensional representation \mathbf{z}_h with the gradient of the abnormality score with respect to \mathbf{z}_h , summed over the feature dimension. In AxialNet, this gradient is equal to the fully connected layer weights for the relevant abnormality (Section 3.4). The mask loss (Section 3.5) is computed using the HiResCAM attention maps and allowed regions \mathcal{G}_{true} to encourage the model to only increase the abnormality score using organs in which that abnormality is found. In this example, the allowed organs are the left lung for mass, the right lung for nodule, and both lungs for pleural effusion.

based explanation methods. Nie *et al.* [42] demonstrate that Guided Backpropagation and DeconvNets perform partial image recovery due to their handling of ReLU nonlinearities and max pooling. Adebayo *et al.* [1] reveal that Guided Backpropagation, Guided Grad-CAM, and Gradient * Input produce convincing explanations even when model parameters have been randomized or when a model has been trained on randomly labeled data. However, saliency mapping and Grad-CAM pass the sanity checks.

Because they are class-specific and produce less noisy explanations than input-level methods, CAM and Grad-CAM form the foundation of numerous methods for weakly supervised localization [32, 59, 57, 28, 60, 31, 58, 21, 2, 22, 12, 13, 37, 36], and have also been widely used in medical imaging applications [35, 44, 9, 50, 45, 41].

We propose a new explanation method, HiResCAM, with connections to Grad-CAM and Gradient * Input that are explored further in Section 3.4. We demonstrate that HiResCAM outperforms Grad-CAM, producing quantita-

tively and qualitatively improved explanations for volumetric medical images.

3. Methods

3.1. Problem setup

Consider a dataset $\{\mathbf{X}, \mathbf{y}\}_{i=1}^N$ where $\mathbf{y}_i \in \{0, 1\}^M$ is a binary vector corresponding to the presence/absence of M abnormalities and $\mathbf{X}_i \in [0, 1]^{405 \times 420 \times 420}$ is a CT volume¹. We wish to predict, in an explainable manner, the labels $\hat{\mathbf{y}}_i$ given a CT volume \mathbf{X}_i , meaning that for any abnormality $m \in \{1, 2, \dots, M\}$ a physician can query the model to retrieve the sub-region within the volume that is most predictive of that abnormality.

We propose a multiple-instance learning architecture that yields per-slice abnormality scores, and we introduce HiResCAM, a novel attention mechanism that provides sub-

¹ $\mathbf{X}_i \in [0, 1]^{135 \times 3 \times 420 \times 420}$ is used when three adjacent slices are grouped to enable use of a feature extractor pre-trained on ImageNet

slice localization. HiResCAM additionally enables calculation of a mask loss that encourages the model to only predict abnormalities using the organs in which they are found, thus improving the quality of model explanations. An overview of our architecture, HiResCAM attention mechanism, and mask loss is provided in Figure 2.

3.2. Modeling

Radiologists typically view CT scans as a stack of axial slices [61], which form horizontal planes through an upright patient. Motivated by this practice, we propose AxialNet, a multiple instance learning architecture that facilitates determination of which axial slices contribute the most to prediction of each abnormality, and enables the most interpretable use of HiResCAM. First, a 2D CNN is applied to each CT slice. The CNN’s parameters are shared across slices (Figure 2), an approach that has been previously successful in CT analysis [18, 38, 48]. The low-dimensional representation produced by the CNN for the h^{th} slice is termed $\mathbf{z}_h \in \mathbb{R}^{F \times D_1 \times D_2}$ with F features, width D_1 , and depth D_2 . It will be used in the proposed attention mechanism HiResCAM as well as the proposed mask loss. Scores c for all M abnormalities are produced from each \mathbf{z}_h , using a fully-connected layer with parameters shared across all CT slices. One row \mathbf{w}_m of the fully connected layer weight matrix corresponds to one abnormality, meaning that the score for the h^{th} slice and m^{th} abnormality is $c_{mh} = \mathbf{w}_m \mathbf{z}_h + b_m$.

The matrix of all per-slice abnormality scores $\mathbf{C} \in \mathbb{R}^{M \times H}$ provides model explainability by illustrating which axial slices contribute most to the prediction of each abnormality.

The final whole-volume abnormality score s_m is produced for each abnormality by averaging the per-slice abnormality scores: $s_m = \frac{1}{H} \sum_{h=1}^H \mathbf{w}_m \mathbf{z}_h + b_m$. Finally, the whole-volume predicted probability \hat{y}_m for the m^{th} abnormality is calculated from the whole-volume score s_m using the sigmoid function $\hat{y}_m = \sigma(s_m) = \frac{1}{1+e^{-s_m}}$.

For each observation we optimize the expected multi-label cross entropy objective, requiring only whole-volume abnormality labels:

$$\mathcal{L}_{class} = -\frac{1}{M} \sum_{m=1}^M [y_m \log \hat{y}_m + (1 - y_m) \log(1 - \hat{y}_m)]. \quad (1)$$

3.3. Proposed HiResCAM for abnormality-specific attention

We propose an attention mechanism, High-Resolution Class Activation Mapping (HiResCAM), which produces for every abnormality $m = 1, \dots, M$ an abnormality-specific attention map $\hat{\mathcal{A}}_m \in \mathbb{R}^{H \times D_1 \times D_2}$, i.e. attention

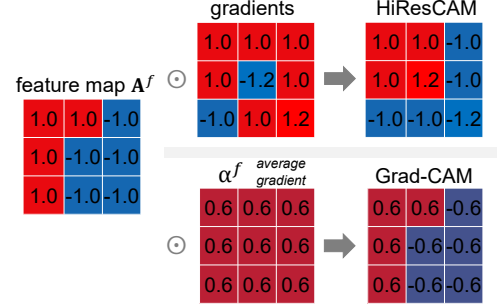


Figure 3. 2D example of how HiResCAM addresses the limitation of the gradient averaging step in Grad-CAM. The Grad-CAM attention map (equation(3)) matches the relative magnitudes and positive-negative pattern of the original feature map (the “inverted red L shape” in this example), even though the gradients suggest that some elements should be re-scaled and/or change sign. HiResCAM (equation (4)) does not average over the gradients and instead element-wise multiplies the feature map with the gradients directly, thereby producing attention that more accurately reflects the model’s computations and emphasizes the most important *locations* for a particular prediction. Best viewed in color.

over the spatial dimensions (excluding the feature dimension F). The abnormality-specific attention maps provide sub-slice localization to further improve explainability and to enable calculation of the mask loss (Section 3.5).

HiResCAM is inspired by the popular attention mechanism Grad-CAM [49], and is designed to address a limitation of the Grad-CAM averaging step. In Grad-CAM, feature map importance weights α^f are calculated by averaging gradients over the spatial dimensions of the low-dimensional CT representation. Such averaging enables Grad-CAM to be a generalization of Class Activation Mapping (CAM) [65]. However, the averaging also limits the extent to which the final visualization depicts the locations within the image that the model is using to make predictions.

Figure 3 illustrates the fundamental problem: each $\alpha^f \mathbf{A}^f$ subcomponent of the final Grad-CAM attention map must always match the relative magnitudes of the feature map \mathbf{A}^f , and either (a) exactly match the positive-negative pattern of the feature map (when α^f is positive), or (b) invert the positive-negative pattern (when α^f is negative). Rescaling and sign changes of individual elements of the feature map are “blurred out.” In HiResCAM, rescaling and sign changes are preserved, producing more high-resolution attention.

Extending Grad-CAM to 3D Data. Grad-CAM was originally described for 2D data [49]. Before introducing the HiResCAM formulation, we describe the extension of Grad-CAM to 3D data.

Recall that s_m is the model’s score for abnormality m before the sigmoid function. To obtain a Grad-CAM attention

map for abnormality m , we first compute the gradient of s_m with respect to a collection of feature maps $\mathbf{A} = \{\mathbf{A}^f\}_{f=1}^F$ produced by a convolutional layer. For volumetric data, the gradient $\frac{\partial s_m}{\partial \mathbf{A}}$ is 4-dimensional $[F, H, D_1, D_2]$.

Next we calculate a vector of importance weights [49] $\alpha_m \in \mathbb{R}^F$ that will be used to re-weight each corresponding feature map \mathbf{A}^f . The importance weights are obtained by global average pooling the gradient over the height, width, and depth dimensions:

$$\alpha_m^f = \frac{1}{HD_1D_2} \sum_{h=1}^H \sum_{d_1=1}^{D_1} \sum_{d_2=1}^{D_2} \frac{\partial s_m}{\partial \mathbf{A}_{hd_1d_2}^f}. \quad (2)$$

The importance weights indicate which features are most relevant to this particular abnormality throughout the volume overall. The Grad-CAM attention map is produced as an importance-weighted combination of the feature maps \mathbf{A}^f :

$$\tilde{\mathcal{A}}_m^{\text{GradCAM}} = \sum_{f=1}^F \alpha_m^f \mathbf{A}^f. \quad (3)$$

Following standard practice for use of Grad-CAM [49], the attention map is then post-processed for better visualization by applying a ReLU and normalizing the attention values to the range $[0, 1]$. This step is intended to ensure that the regions positively associated with a abnormality will be easily visible.

HiResCAM Formulation HiResCAM overcomes the limitation of Grad-CAM illustrated in Figure 3. The first step of HiResCAM is the same as Grad-CAM: compute $\frac{\partial s_m}{\partial \mathbf{A}}$, the gradient of s_m with respect to the feature maps \mathbf{A} .

In the second step of HiResCAM, the attention map is produced by element-wise multiplying the gradient and the feature maps before summing over the feature dimension:

$$\tilde{\mathcal{A}}_m^{\text{HiResCAM}} = \sum_{f=1}^F \frac{\partial s_m}{\partial \mathbf{A}^f} \odot \mathbf{A}^f. \quad (4)$$

The motivation behind HiResCAM is that if the gradients indicate that some elements of the feature map should be scaled or have their sign inverted, then it is more reflective of what the model is computing to perform these operations, rather than to blur the effect of the gradients across each feature map as is done in Grad-CAM.

3.4. HiResCAM intuition: visualizing important image regions

For the most interpretable explanation, HiResCAM should be applied at the last convolutional layer of a CNN that ends in one fully connected layer. In this setup

HiResCAM has an intuitive interpretation: the resulting attention map highlights all *regions* of the image that increase the prediction score. In contrast, Grad-CAM emphasizes the *features* that increase the prediction score, which can result in substantially different explanations.

AxialNet enables the optimally interpretable use of HiResCAM, for it is composed of convolutional layers followed by one fully connected layer. We apply HiResCAM at \mathbf{Z} , the output of the last convolutional layer. The first step of HiResCAM is to calculate the gradient of the abnormality score s_m with respect to \mathbf{Z} . The previous expression for the abnormality score s_m was written in terms of the slices \mathbf{z}_h . To rewrite $s_m = \frac{1}{H} \sum_{h=1}^H \mathbf{w}_m \mathbf{z}_h + b_m$ in terms of \mathbf{Z} overall requires two concatenations. First, define $\mathbf{w}_m^{\text{cat}}$ as the vector resulting from concatenation of the m^{th} -abnormality-specific weights \mathbf{w}_m with themselves H times: $\mathbf{w}_m^{\text{cat}} = \mathbf{w}_m \parallel \mathbf{w}_m \parallel \dots \parallel \mathbf{w}_m$. Next define \mathbf{Z} as the vector resulting from concatenation of all the flattened \mathbf{z}_h representations, $\mathbf{Z} = \mathbf{z}_1 \parallel \mathbf{z}_2 \parallel \dots \parallel \mathbf{z}_H$. Then an alternative expression for the whole volume abnormality score s_m is:

$$s_m = \frac{1}{H} \mathbf{w}_m^{\text{cat}} \mathbf{Z} + b_m. \quad (5)$$

The gradient of the abnormality score s_m with respect to \mathbf{Z} can then be calculated as:

$$\frac{\partial s_m}{\partial \mathbf{Z}} = \frac{\partial}{\partial \mathbf{Z}} \left(\frac{1}{H} \mathbf{w}_m^{\text{cat}} \mathbf{Z} + b_m \right) \quad (6)$$

$$= \frac{1}{H} \mathbf{w}_m^{\text{cat}}. \quad (7)$$

We then follow equation (4) to calculate the HiResCAM attention map as follows:

$$\tilde{\mathcal{A}}_m^{\text{HiResCAM}} = \sum_{f=1}^F \frac{\partial s_m}{\partial \mathbf{Z}} \odot \mathbf{Z}. \quad (8)$$

Substituting in equation (7) for $\frac{\partial s_m}{\partial \mathbf{Z}}$, we obtain

$$\tilde{\mathcal{A}}_m^{\text{HiResCAM}} = \sum_{f=1}^F \frac{1}{H} \mathbf{w}_m^{\text{cat}} \odot \mathbf{Z}. \quad (9)$$

The element-wise multiplication $\mathbf{w}_m^{\text{cat}} \odot \mathbf{Z}$ in the HiResCAM attention map expression is the intermediate computation in calculating $\mathbf{w}_m^{\text{cat}} \mathbf{Z}$, which in turn is a direct contributor to the abnormality score $s_m = (\frac{1}{H} \mathbf{w}_m^{\text{cat}} \mathbf{Z}) + b_m$.

Therefore, the large positive elements of the HiResCAM attention map $\tilde{\mathcal{A}}_m$ that show up as abnormality-relevant image regions correspond to regions which directly increase the abnormality score. Similarly, negative elements of the HiResCAM attention map are direct contributors to a lower abnormality score. That means the HiResCAM attention

map can be interpreted as showing exactly which parts of the scan contributed most to the abnormality score.

Grad-CAM intuition: visualizing features, not regions. Grad-CAM does not directly visualize important regions. The intuitive interpretation of HiResCAM does not apply, even if Grad-CAM is used at the last convolutional layer. To calculate the Grad-CAM explanation at the level of \mathbf{Z} , we first follow equation (2) to obtain the importance weights:

$$\alpha_m^f = \frac{1}{HD_1D_2} \sum_{h=1}^H \sum_{d_1=1}^{D_1} \sum_{d_2=1}^{D_2} \frac{1}{H} \mathbf{w}_m^{cat}. \quad (10)$$

These importance weights are then multiplied against the corresponding feature maps of $\mathbf{Z} = \{\mathbf{z}^f\}_{f=1}^F$. Essentially this means that all the fully connected layer weights corresponding to a given feature map are averaged together and then the resulting scalar is multiplied against the feature map. The overall effect is to emphasize the *features* that contribute most to the prediction across the entire image, even if in the model’s computations these important features are only actually contributing to the score in a few focal areas.

Thus, while HiResCAM produces explanations based on the most important image *regions*, Grad-CAM produces explanations based on the most important image *features*. Important features and important regions can coincide, but do not always coincide. We will show that HiResCAM outperforms Grad-CAM at correct region localization in CT scans, while Grad-CAM yields more expansive explanations in natural images.

HiResCAM: faithful, computationally efficient class-specific explanations The preceding analysis demonstrated HiResCAM’s relationship to Grad-CAM. HiResCAM is also related to Gradient * Input, thus providing a conceptual link between Grad-CAM and Gradient * Input. If HiResCAM were to be applied at the level of the input image, it would be equivalent to Gradient * Input. While the “level of application” is a simple distinction, it has several critical implications that, to the best of our knowledge, have not been explored previously in the literature. First, HiResCAM explanations are clean and class-specific, whereas Gradient * Input and other pixel-space explanations produce visualizations that are too noisy to be class-specific [49]. Second, HiResCAM is not susceptible to the same issue that caused Gradient * Input to fail basic sanity checks [1]: namely, HiResCAM does not involve element-wise multiplication with the raw input image. Third, when HiResCAM is used as recommended in the previous section, the HiResCAM explanations can be seamlessly integrated into model training in a computationally efficient manner, a consideration that is particularly important when working with massive CT volumes. Equation (9) can be calculated during the forward pass, meaning

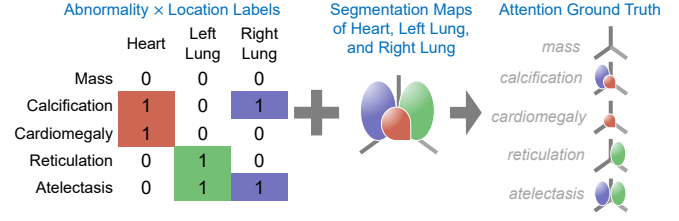


Figure 4. Schematic of the attention ground truth creation. By combining the location \times abnormality labels and the organ segmentation masks, it is possible to define “allowed regions” for each abnormality with no manual labor.

that no extra backward passes are needed. Finally, because the HiResCAM explanation is in a low-dimensional space, computing a loss on it (Section 3.5) requires orders of magnitude fewer computations than if the same loss were calculated in input space.

3.5. Proposed mask loss

We propose a mask loss that leverages HiResCAM to improve the quality of explanations by restricting the abnormality-specific attention to allowed regions for each abnormality m . Given the model’s predicted attention $\tilde{\mathcal{A}} \in \mathbb{R}^{M \times H \times D_1 \times D_2}$ and a binary mask $\mathcal{G}_{true} \in \{0, 1\}^{M \times H \times D_1 \times D_2}$ which defines an allowed region for the attention for each abnormality, the mask loss is calculated as follows (using \tilde{a}_i to access all MHD_1D_2 elements of $\tilde{\mathcal{A}}$):

$$\mathcal{L}_{mask} = - \sum_{i: \mathcal{G}_{true}=0} \log(1 - \tilde{a}_i). \quad (11)$$

The proposed mask loss is conceptually half of a segmentation loss [30], applied in a low-dimensional space. To minimize the mask loss the model must not increase the abnormality score using forbidden regions. Further justification for this choice of mask loss is provided in the Supplementary Material. The overall loss, incorporating the classification loss (equation 1), is then $\mathcal{L}_{total} = \mathcal{L}_{class} + \lambda \mathcal{L}_{mask}$.

Creating an attention ground truth The primary barrier to computing the mask loss is obtaining \mathcal{G}_{true} which specifies the allowed regions for each abnormality. Manually creating \mathcal{G}_{true} would require months of expert manual labor. Therefore, we develop an efficient approach for obtaining \mathcal{G}_{true} computationally. First, we expand the previously described SARLE [18] natural language processing method with location vocabulary, in order to automatically identify the location of each abnormality in the free text CT reports. Next, we develop an unsupervised multi-organ segmentation pipeline using morphological image processing to define segmentation maps of the right lung, left lung, and heart/mediastinum in each volume individually. Randomly

selected examples of the lung segmentation are shown in the Supplementary Material. The combination of the location \times abnormality labels and the organ segmentation masks enables determination of an “allowed region” for each abnormality as illustrated in Figure 4. Further details are provided in the Supplementary Material.

4. Experiments

Datasets. RAD-ChestCT [18] is a data set of 36,316 CT volumes with 83 whole-volume abnormality labels. We focus on $M = 80$ labels relevant to the lungs and heart/mediastinum, detailed in the Supplementary Material. To quantify the effect of HiResCAM and the mask loss on explanation quality, we train AxialNet on the full data set. Because it takes ≥ 1 week to train a model on the full RAD-ChestCT data set, for architecture comparisons and ablation studies we use a predefined subset [18] of 2,000 training scans and 1,000 validation scans intended for this purpose.

PASCAL VOC 2012 [20] is a data set of 2D RGB natural images with segmentation maps of 20 classes. Following prior work [58], we combine PASCAL VOC 2012 with SBD [26] to create an augmented training set of 7,087 images. We only use whole-image labels for training classification models.

Implementation details. The per-slice CNN in AxialNet consists of a 2D ResNet-18 [27] pretrained on ImageNet [16] and refined during training on CTs, followed by custom convolutional layers. All models are implemented in PyTorch. Models were trained using stochastic gradient descent with momentum 0.99 and learning rate 10^{-3} . Whole-dataset models were trained on an NVIDIA Tesla V100 GPU with 32 GiB of memory. All code will be made publicly available.

OrganIoU: a metric for explanation quality. There is no standard method for quantitatively evaluating the quality of a neural network explanation [4]. Weakly supervised segmentation methods are often evaluated with intersection over union (IoU), which requires ground truth class-specific segmentation masks that are not available in any multilabel volumetric medical imaging data set. Therefore we propose OrganIoU, a metric that equals 1 when the model has assigned all abnormality attention within the allowed regions for that abnormality, and equals 0 when the model has only assigned attention to forbidden regions. The OrganIoU is calculated using the model’s predicted attention $\hat{A} \in \mathbb{R}^{M \times H \times D_1 \times D_2}$ and the attention ground truth $G_{true} \in \{0, 1\}^{M \times H \times D_1 \times D_2}$. The predicted attention is binarized with different thresholds and the optimal threshold chosen for each abnormality on the validation set. Define *allowed* as the sum of all predicted attention values where $G_{true} = 1$ and *forbidden* as the sum of all predicted attention values where $G_{true} = 0$. Then $\text{OrganIoU} = \frac{\text{allowed}}{\text{allowed} + \text{forbidden}}$.

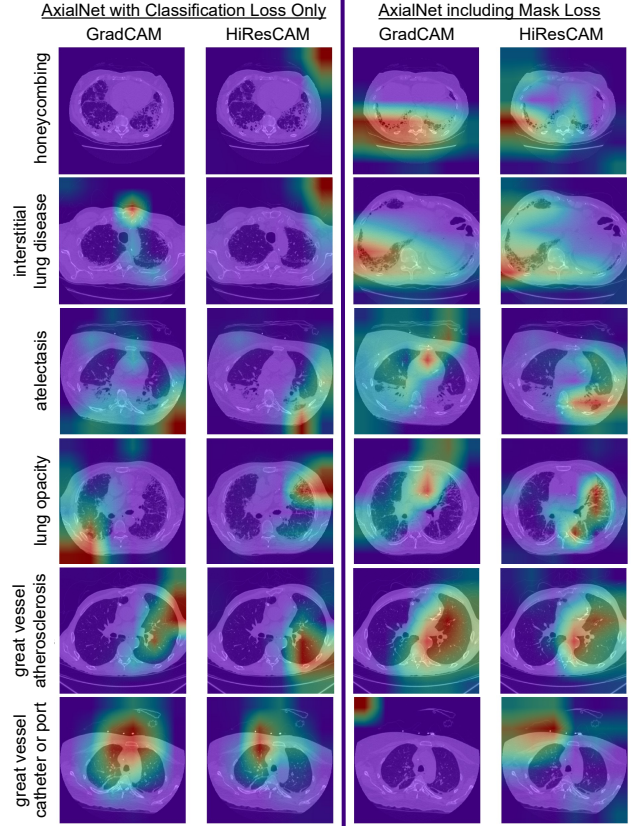


Figure 5. Qualitative results illustrating the effect of the mask loss as well as the difference between Grad-CAM and HiResCAM explanations for the same model. The highest scoring slice is shown for each abnormality. The top two rows exemplify cases where the mask loss model produces a correct explanation while the model trained without the mask loss fails. In the middle two rows, only the HiResCAM mask loss explanation is correct, while the Grad-CAM mask loss explanation creates the impression that the model attended to the wrong organ. For the final row, a great vessel catheter was identified via its tail outside the body rather than its presence inside the great vessel. Best viewed in color, with zoom.

Alternative models and ablation study AxialNet outperforms the alternative models CTNet, 3DConv, and BodyConv (Table 1) on classification and localization. HiResCAM also yields better performance than GradCAM for every alternative model. The ablation study emphasizes the benefit of average pooling (vs. MaxPool), use of a pre-trained ResNet (vs. RandInitResNet), and inclusion of the custom convolution layers (vs. NoCustomConv).

Explainability in 3D medical images. The mask loss and HiResCAM attention mechanism in AxialNet produce state-of-the-art performance, with a synergistic effect that results in a 37% improvement ($20.1 \rightarrow 27.6$ OrganIoU) in explanation quality overall (Table 2). The qualitative performance shown in Figure 5 further emphasizes the benefit of using the mask loss and HiResCAM for the most accu-

Architecture Comparison and Ablation Study

Model		AUROC	OrganIoU	
			GradCAM	HiResCAM
Alternative Models	CTNet [18]	66.3	-	-
	3DConv [18]	53.8	3.3	4.5
	BodyConv [18]	50.2	0.0	14.6
Ablation	MaxPool	65.5	9.3	10.9
	RandInitResNet	63.1	15.1	14.1
	NoCustomConv	56.5	10.0	19.7
Proposed	AxialNet	67.5	18.7	21.5

Table 1. Validation set classification performance (median AUROC) and localization performance (mean OrganIoU) for alternative models and ablated versions of AxialNet, using the predefined 2,000 train/1,000 val subset [18] for computational feasibility. OrganIoU was calculated at the last convolutional layer of all models. No OrganIoU could be calculated for CTNet as the spatial relationship between the output of the last convolutional layer and the input has been disrupted due to convolution over features.

rate explanations. The mask loss model of the middle rows, for lung opacity and atelectasis (collapsed lung tissue), are a particularly interesting case because the Grad-CAM visualization creates the false impression that the model has focused on the wrong organ - the heart instead of the lungs. In contrast, the region-focused HiResCAM attention shows that the model is actually looking at lung tissue as it should (these slices were verified by a physician trained in analysis of CT volumes). We hypothesize that Grad-CAM’s focus on the wrong organ arises because both opacities and atelectasis are “light grey” abnormalities, and may activate features that detect this “light grey” quality; unfortunately, the heart is more “light grey” than any adjacent lung tissue, so feature-focused Grad-CAM fixates incorrectly on the heart.

Case study. The label “great vessel atherosclerosis” exemplifies how the mask loss discourages exploitation of confounding variables. Obesity is a known risk factor for atherosclerosis [62], which the baseline model leverages by focusing on body wall fat content. Figure 1 depicts an overweight patient for which both the baseline and mask loss models predict high likelihood of atherosclerosis (probabilities 170% and 183% above the average prediction for this label, respectively). Figure 5 row 5 shows a thinner patient with great vessel atherosclerosis; the baseline model again focuses on the body wall, with a score only 108% above average, while the mask loss model focuses on the great vessel itself and produces a score 183% above average in spite of the patient’s thinner body habitus.

HiResCAM vs. Grad-CAM in natural images. Interestingly, for natural images Grad-CAM yields more expansive explanations (Figure 6) that lead to higher IoU. For a VGG-16 classifier trained on PASCAL VOC 2012, the mean validation set IoU of the raw explanations is 28.5 for HiResCAM vs. 33.3 for Grad-CAM. We hypothesize that

AxialNet Test Set OrganIoU: Effect of Attention Mechanism & Mask Loss

		\mathcal{L}_{class} only		\mathcal{L}_{class} & \mathcal{L}_{mask}		Summary
		%	Grad	HiRes	Grad	HiRes
focal	53	22.6	20.1	27.2	29.6	+31.3%
diffuse	47	17.3	21.4	14.8	25.3	+46.1%
biological	89	20.3	20.9	21.6	27.6	+36.1%
intervention	11	18.8	19.3	19.8	27.6	+46.6%
overall	100	20.1	20.7	21.4	27.6	+37.2%

Table 2. The RAD-ChestCT test set mean OrganIoU quantifying explanation quality. Grad = Grad-CAM, HiRes=HiResCAM. The proposed mask loss and HiResCAM attention mechanism together yield state-of-the-art performance with a 37% improvement in explanation quality (20.1 \rightarrow 27.6 OrganIoU). Diffuse abnormalities (*e.g.* emphysema, interstitial lung disease) improve more than focal abnormalities (*e.g.* nodule, mass). Intervention-related abnormalities (*e.g.* pacemaker, stent) improve more than biological abnormalities (*e.g.* nodule, emphysema). The full list of abnormalities in each concept group is provided in the Supplementary Material. There are 7,209 test set volumes, which cumulatively include 61,780 abnormalities; the Percent (%) column specifies the percent of abnormalities in each concept group.

in natural images, particular features may correlate highly with particular classes (*e.g.* fur texture with animals, or metal texture with cars); therefore visualizing these features produces a broader highlight of the relevant class. However, in medical images, different abnormalities can look so similar to one another that it can be challenging even for experts to distinguish them [18], so it is unlikely that any single feature would be highly predictive of an abnormality on its own. Grad-CAM’s focus on features thus risks switching the attention to the wrong anatomical structure as exemplified in Figure 5. Formal investigation into the cause of this phenomenon is an interesting direction for future work.

We propose that HiResCAM is particularly applicable in medical imaging, where understanding the precise contributing region of the image is paramount, while Grad-CAM may be more useful for tasks like weakly supervised segmentation in natural images, where “expanded” attention maps serve as better seeds [11].

5. Conclusion

We present HiResCAM, a class-specific, region-focused attention mechanism that highlights the locations that contribute most towards each abnormality prediction. We propose a mask loss that leverages HiResCAM and automatically obtained allowed regions to encourage the model to predict abnormalities from only the organs in which they appear. Together, HiResCAM and the mask loss result in a 37% improvement in explanation quality, demonstrating state-of-the-art performance on explainable multiple abnormality prediction in 3D medical images.

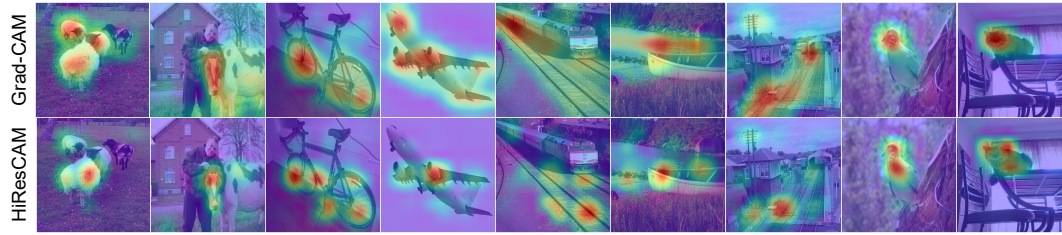


Figure 6. Qualitative results of a VGG-16 classifier on the PASCAL VOC 2012 val set, illustrating the tendency of HiResCAM to produce more focused attention. Best viewed in color with zoom.

Acknowledgements. The authors would like to thank the Duke Protected Analytics Computing Environment (PACE), particularly Mike Newton and Charley Kneifel, PhD, for providing the computing resources and GPUs needed to complete this work. The authors also thank Paidamoyo Chapfuwa, MS, for thoughtful comments on the manuscript, David Dov, PhD, for discussion of multiple instance learning, and Geoffrey D. Rubin, MD, FACR, for inspecting the CT slices in Figures 1 and 5.

References

- [1] Julius Adebayo, Justin Gilmer, Michael Muelly, Ian Goodfellow, Moritz Hardt, and Been Kim. Sanity checks for saliency maps. In *Advances in Neural Information Processing Systems*, pages 9505–9515, 2018. [3](#), [6](#)
- [2] Jiwoon Ahn and Suha Kwak. Learning pixel-level semantic affinity with image-level supervision for weakly supervised semantic segmentation. In *Proceedings of the IEEE Conference on Computer Vision and Pattern Recognition*, pages 4981–4990, 2018. [3](#)
- [3] Alan Alexander, Adam Jiang, Cara Ferreira, and Delphine Zurkiya. An intelligent future for medical imaging: a market outlook on artificial intelligence for medical imaging. *Journal of the American College of Radiology*, 17(1):165–170, 2020. [1](#)
- [4] Marco Ancona, Enea Ceolini, Cengiz Öztireli, and Markus Gross. Gradient-based attribution methods. In *Explainable AI: Interpreting, Explaining and Visualizing Deep Learning*, pages 169–191. Springer, 2019. [1](#), [2](#), [7](#)
- [5] Marios Anthimopoulos, Stergios Christodoulidis, Lukas Ebner, Andreas Christe, and Stavroula Mougiakakou. Lung pattern classification for interstitial lung diseases using a deep convolutional neural network. *IEEE transactions on medical imaging*, 35(5):1207–1216, 2016. [2](#)
- [6] Diego Ardila, Atilla P Kiraly, Sujeeth Bharadwaj, Bokyung Choi, Joshua J Reicher, Lily Peng, Daniel Tse, Mozziyar Etemadi, Wenxing Ye, Greg Corrado, et al. End-to-end lung cancer screening with three-dimensional deep learning on low-dose chest computed tomography. *Nature medicine*, 25(6):954–961, 2019. [2](#)
- [7] Sebastian Bach, Alexander Binder, Grégoire Montavon, Frederick Klauschen, Klaus-Robert Müller, and Wojciech Samek. On pixel-wise explanations for non-linear classifier decisions by layer-wise relevance propagation. *PloS one*, 10(7):e0130140, 2015. [2](#)
- [8] David Balduzzi, Marcus Frean, Lennox Leary, JP Lewis, Kurt Wan-Duo Ma, and Brian McWilliams. The shattered gradients problem: If resnets are the answer, then what is the question? *arXiv preprint arXiv:1702.08591*, 2017. [2](#)
- [9] Ivo M Baltruschat, Hannes Nickisch, Michael Grass, Tobias Knopp, and Axel Saalbach. Comparison of deep learning approaches for multi-label chest x-ray classification. *Scientific reports*, 9(1):1–10, 2019. [3](#)
- [10] David Bermejo-Peláez, Samuel Y Ash, George R Washko, Raúl San José Estépar, and María J Ledesma-Carbayo. Classification of interstitial lung abnormality patterns with an ensemble of deep convolutional neural networks. *Scientific reports*, 10(1):1–15, 2020. [2](#)
- [11] Lyndon Chan, Mahdi S Hosseini, and Konstantinos N Plataniotis. A comprehensive analysis of weakly-supervised semantic segmentation in different image domains. *International Journal of Computer Vision*, pages 1–24, 2020. [8](#)
- [12] Yu-Ting Chang, Qiaosong Wang, Wei-Chih Hung, Robinson Piramuthu, Yi-Hsuan Tsai, and Ming-Hsuan Yang. Mixup-cam: Weakly-supervised semantic segmentation via uncertainty regularization. *arXiv preprint arXiv:2008.01201*, 2020. [3](#)
- [13] Yu-Ting Chang, Qiaosong Wang, Wei-Chih Hung, Robinson Piramuthu, Yi-Hsuan Tsai, and Ming-Hsuan Yang. Weakly-supervised semantic segmentation via sub-category exploration. In *Proceedings of the IEEE/CVF Conference on Computer Vision and Pattern Recognition*, pages 8991–9000, 2020. [3](#)
- [14] Stergios Christodoulidis, Marios Anthimopoulos, Lukas Ebner, Andreas Christe, and Stavroula Mougiakakou. Multi-source transfer learning with convolutional neural networks for lung pattern analysis. *IEEE journal of biomedical and health informatics*, 21(1):76–84, 2016. [2](#)
- [15] Diana Crossley, Mary Renton, Muhammad Khan, Emma V Low, and Alice M Turner. Ct densitometry in emphysema: a systematic review of its clinical utility. *International journal of chronic obstructive pulmonary disease*, 13:547, 2018. [2](#)
- [16] Jia Deng, Wei Dong, Richard Socher, Li-Jia Li, Kai Li, and Li Fei-Fei. Imagenet: A large-scale hierarchical image database. In *2009 IEEE conference on computer vision and pattern recognition*, pages 248–255. Ieee, 2009. [7](#)
- [17] Ashis Kumar Dhara, Sudipta Mukhopadhyay, Anirvan Dutta, Mandeep Garg, and Niranjana Khandelwal. A combination of shape and texture features for classification of pulmonary nodules in lung ct images. *Journal of digital imaging*, 29(4):466–475, 2016. [2](#)
- [18] Rachel Lea Draelos, David Dov, Maciej A. Mazurowski, Joseph Y. Lo, Ricardo Henao, Geoffrey D. Rubin, and

- Lawrence Carin. Machine-learning-based multiple abnormality prediction with large-scale chest computed tomography volumes. *Medical Image Analysis*, 67, 2021. 2, 4, 6, 7, 8
- [19] Rachael M Edwards, J David Godwin, Dan S Hippe, and Gregory Kicska. A quantitative approach to distinguish pneumonia from atelectasis using computed tomography attenuation. *Journal of computer assisted tomography*, 40(5):746–751, 2016. 2
- [20] Mark Everingham, Luc Van Gool, Christopher KI Williams, John Winn, and Andrew Zisserman. The pascal visual object classes (voc) challenge. *International journal of computer vision*, 88(2):303–338, 2010. 7
- [21] Junsong Fan, Zhaoxiang Zhang, Chunfeng Song, and Tieniu Tan. Learning integral objects with intra-class discriminator for weakly-supervised semantic segmentation. In *Proceedings of the IEEE/CVF Conference on Computer Vision and Pattern Recognition*, pages 4283–4292, 2020. 3
- [22] Junsong Fan, Zhaoxiang Zhang, Tieniu Tan, Chunfeng Song, and Jun Xiao. Cian: Cross-image affinity net for weakly supervised semantic segmentation. In *Proceedings of the AAAI Conference on Artificial Intelligence*, volume 34, pages 10762–10769, 2020. 3
- [23] T Franquet. Imaging of pneumonia: trends and algorithms. *European Respiratory Journal*, 18(1):196–208, 2001. 2
- [24] Mingchen Gao, Ulas Bagci, Le Lu, Aaron Wu, Mario Buty, Hoo-Chang Shin, Holger Roth, Georgios Z Papadakis, Adrien Depeursinge, Ronald M Summers, et al. Holistic classification of ct attenuation patterns for interstitial lung diseases via deep convolutional neural networks. *Computer Methods in Biomechanics and Biomedical Engineering: Imaging & Visualization*, 6(1):1–6, 2018. 2
- [25] Mingchen Gao, Ziyue Xu, Le Lu, Adam P Harrison, Ronald M Summers, and Daniel J Mollura. Multi-label deep regression and unordered pooling for holistic interstitial lung disease pattern detection. In *International Workshop on Machine Learning in Medical Imaging*, pages 147–155. Springer, 2016. 2
- [26] Bharath Hariharan, Pablo Arbeláez, Lubomir Bourdev, Subhransu Maji, and Jitendra Malik. Semantic contours from inverse detectors. In *2011 International Conference on Computer Vision*, pages 991–998. IEEE, 2011. 7
- [27] Kaiming He, Xiangyu Zhang, Shaoqing Ren, and Jian Sun. Deep residual learning for image recognition. In *Proceedings of the IEEE conference on computer vision and pattern recognition*, pages 770–778, 2016. 7
- [28] Zilong Huang, Xinggang Wang, Jiasi Wang, Wenyu Liu, and Jingdong Wang. Weakly-supervised semantic segmentation network with deep seeded region growing. In *Proceedings of the IEEE Conference on Computer Vision and Pattern Recognition*, pages 7014–7023, 2018. 3
- [29] Stephen M Humphries, Aleena M Notary, Juan Pablo Centeno, Matthew J Strand, James D Crapo, Edwin K Silverman, David A Lynch, and Genetic Epidemiology of COPD (COPDGene) Investigators. Deep learning enables automatic classification of emphysema pattern at ct. *Radiology*, 294(2):434–444, 2020. 2
- [30] Shruti Jadon. A survey of loss functions for semantic segmentation. *arXiv preprint arXiv:2006.14822*, 2020. 6
- [31] Peng-Tao Jiang, Qibin Hou, Yang Cao, Ming-Ming Cheng, Yunchao Wei, and Hong-Kai Xiong. Integral object mining via online attention accumulation. In *Proceedings of the IEEE International Conference on Computer Vision*, pages 2070–2079, 2019. 3
- [32] Alexander Kolesnikov and Christoph H Lampert. Seed, expand and constrain: Three principles for weakly-supervised image segmentation. In *European conference on computer vision*, pages 695–711. Springer, 2016. 3
- [33] Sebastian Lapuschkin, Alexander Binder, Grégoire Montavon, Klaus-Robert Müller, and Wojciech Samek. Analyzing classifiers: Fisher vectors and deep neural networks. In *Proceedings of the IEEE Conference on Computer Vision and Pattern Recognition*, pages 2912–2920, 2016. 2
- [34] Sebastian Lapuschkin, Stephan Wäldchen, Alexander Binder, Grégoire Montavon, Wojciech Samek, and Klaus-Robert Müller. Unmasking clever hans predictors and assessing what machines really learn. *Nature communications*, 10(1):1–8, 2019. 2
- [35] Hyunkwang Lee, Sehyo Yune, Mohammad Mansouri, Myeongchan Kim, Shahein H Tajmir, Claude E Guerrier, Sarah A Ebert, Stuart R Pomerantz, Javier M Romero, Shahrir Kamalian, et al. An explainable deep-learning algorithm for the detection of acute intracranial haemorrhage from small datasets. *Nature Biomedical Engineering*, 3(3):173, 2019. 3
- [36] Jungbeom Lee, Eunji Kim, Sungmin Lee, Jangho Lee, and Sungroh Yoon. Ficklenet: Weakly and semi-supervised semantic image segmentation using stochastic inference. In *Proceedings of the IEEE conference on computer vision and pattern recognition*, pages 5267–5276, 2019. 3
- [37] Kunpeng Li, Ziyang Wu, Kuan-Chuan Peng, Jan Ernst, and Yun Fu. Tell me where to look: Guided attention inference network. In *Proceedings of the IEEE Conference on Computer Vision and Pattern Recognition*, pages 9215–9223, 2018. 3
- [38] Lin Li, Lixin Qin, Zeguo Xu, Youbing Yin, Xin Wang, Bin Kong, Junjie Bai, Yi Lu, Zhenghan Fang, Qi Song, et al. Using artificial intelligence to detect covid-19 and community-acquired pneumonia based on pulmonary ct: evaluation of the diagnostic accuracy. *Radiology*, 296(2), 2020. 4
- [39] Xiang Li, James H Thrall, Subba R Digumarthy, Manudeep K Kalra, Pari V Pandharipande, Bowen Zhang, Chayanin Nitiwarangkul, Ramandeep Singh, Ruhani Doda Khera, and Quanzheng Li. Deep learning-enabled system for rapid pneumothorax screening on chest ct. *European journal of radiology*, 120:108692, 2019. 2
- [40] Zhan Wei Lim, Mong Li Lee, Wynne Hsu, and Tien Yin Wong. Building trust in deep learning system towards automated disease detection. In *Proceedings of the AAAI Conference on Artificial Intelligence*, volume 33, pages 9516–9521, 2019. 1
- [41] Michael T Lu, Alexander Ivanov, Thomas Mayrhofer, Ahmed Hosny, Hugo JWL Aerts, and Udo Hoffmann. Deep learning to assess long-term mortality from chest radio-

- graphs. *JAMA network open*, 2(7):e197416–e197416, 2019. 3
- [42] Weili Nie, Yang Zhang, and Ankit Patel. A theoretical explanation for perplexing behaviors of backpropagation-based visualizations. *arXiv preprint arXiv:1805.07039*, 2018. 2, 3
- [43] Anastasia Oikonomou and Panos Prassopoulos. Ct imaging of blunt chest trauma. *Insights into imaging*, 2(3):281–295, 2011. 2
- [44] Harsh Panwar, PK Gupta, Mohammad Khubeb Siddiqui, Ruben Morales-Menendez, Prakhar Bhardwaj, and Vaishnavi Singh. A deep learning and grad-cam based color visualization approach for fast detection of covid-19 cases using chest x-ray and ct-scan images. *Chaos, Solitons & Fractals*, 140:110190, 2020. 3
- [45] F Pasa, V Golkov, F Pfeiffer, D Cremers, and D Pfeiffer. Efficient deep network architectures for fast chest x-ray tuberculosis screening and visualization. *Scientific reports*, 9(1):1–9, 2019. 3
- [46] Shine Raju, Subha Ghosh, and Atul C Mehta. Chest ct signs in pulmonary disease: a pictorial review. *Chest*, 151(6):1356–1374, 2017. 2
- [47] Marco Tulio Ribeiro, Sameer Singh, and Carlos Guestrin. ” why should i trust you?” explaining the predictions of any classifier. In *Proceedings of the 22nd ACM SIGKDD international conference on knowledge discovery and data mining*, pages 1135–1144, 2016. 1
- [48] Khaled Saab, Jared Dunnmon, Roger Goldman, Alex Ratner, Hersh Sagreiya, Christopher Ré, and Daniel Rubin. Doubly weak supervision of deep learning models for head ct. In *International Conference on Medical Image Computing and Computer-Assisted Intervention*, pages 811–819. Springer, 2019. 4
- [49] Ramprasaath R Selvaraju, Michael Cogswell, Abhishek Das, Ramakrishna Vedantam, Devi Parikh, and Dhruv Batra. Grad-cam: Visual explanations from deep networks via gradient-based localization. In *Proceedings of the IEEE international conference on computer vision*, pages 618–626, 2017. 2, 4, 5, 6
- [50] Yan Shen and Mingchen Gao. Dynamic routing on deep neural network for thoracic disease classification and sensitive area localization. In *International Workshop on Machine Learning in Medical Imaging*, pages 389–397. Springer, 2018. 3
- [51] Yiwey Shieh and Martin Bohnenkamp. Low-dose ct scan for lung cancer screening: clinical and coding considerations. *Chest*, 152(1):204–209, 2017. 2
- [52] Avanti Shrikumar, Peyton Greenside, Anna Shcherbina, and Anshul Kundaje. Not just a black box: Learning important features through propagating activation differences. *arXiv preprint arXiv:1605.01713*, 2016. 2
- [53] Karen Simonyan, Andrea Vedaldi, and Andrew Zisserman. Deep inside convolutional networks: Visualising image classification models and saliency maps. *ICLR*, 2014. 2
- [54] Jost Tobias Springenberg, Alexey Dosovitskiy, Thomas Brox, and Martin Riedmiller. Striving for simplicity: The all convolutional net. *arXiv preprint arXiv:1412.6806*, 2014. 2
- [55] Simon LF Walsh, Lucio Calandriello, Mario Silva, and Nicola Sverzellati. Deep learning for classifying fibrotic lung disease on high-resolution computed tomography: a case-cohort study. *The Lancet Respiratory Medicine*, 6(11):837–845, 2018. 2
- [56] Chenglong Wang, Takayasu Moriya, Yuichiro Hayashi, Holger Roth, Le Lu, Masahiro Oda, Hirotsugu Ohkubo, and Kensaku Mori. Weakly-supervised deep learning of interstitial lung disease types on ct images. In *Medical Imaging 2019: Computer-Aided Diagnosis*, volume 10950, page 109501H. International Society for Optics and Photonics, 2019. 2
- [57] Xiang Wang, Shaodi You, Xi Li, and Huimin Ma. Weakly-supervised semantic segmentation by iteratively mining common object features. In *Proceedings of the IEEE conference on computer vision and pattern recognition*, pages 1354–1362, 2018. 3
- [58] Yude Wang, Jie Zhang, Meina Kan, Shiguang Shan, and Xilin Chen. Self-supervised equivariant attention mechanism for weakly supervised semantic segmentation. In *Proceedings of the IEEE/CVF Conference on Computer Vision and Pattern Recognition*, pages 12275–12284, 2020. 3, 7
- [59] Yunchao Wei, Jiashi Feng, Xiaodan Liang, Ming-Ming Cheng, Yao Zhao, and Shuicheng Yan. Object region mining with adversarial erasing: A simple classification to semantic segmentation approach. In *Proceedings of the IEEE conference on computer vision and pattern recognition*, pages 1568–1576, 2017. 3
- [60] Yunchao Wei, Huaxin Xiao, Honghui Shi, Zequn Jie, Jiashi Feng, and Thomas S Huang. Revisiting dilated convolution: A simple approach for weakly-and semi-supervised semantic segmentation. In *Proceedings of the IEEE Conference on Computer Vision and Pattern Recognition*, pages 7268–7277, 2018. 3
- [61] P Whiting, N Singatullina, and JH Rosser. Computed tomography of the chest: I. basic principles. *Bja Education*, 15(6):299–304, 2015. 4
- [62] Hye Jin Yoo and Kyung Mook Choi. Adipokines as a novel link between obesity and atherosclerosis. *World journal of diabetes*, 5(3):357, 2014. 8
- [63] John R Zech, Marcus A Badgeley, Manway Liu, Anthony B Costa, Joseph J Titano, and Eric Karl Oermann. Variable generalization performance of a deep learning model to detect pneumonia in chest radiographs: a cross-sectional study. *PLoS medicine*, 15(11):e1002683, 2018. 1
- [64] Matthew D Zeiler and Rob Fergus. Visualizing and understanding convolutional networks. In *European conference on computer vision*, pages 818–833. Springer, 2014. 2
- [65] Bolei Zhou, Aditya Khosla, Agata Lapedriza, Aude Oliva, and Antonio Torralba. Learning deep features for discriminative localization. In *Proceedings of the IEEE conference on computer vision and pattern recognition*, pages 2921–2929, 2016. 1, 2, 4